Int. J. Multiphase Flow Vol. 14, No. 2, pp. 217–232, 1988
Printed in Great Britain.

0301-9322/88 $3.00 + 0.00

DRAG COEFFICIENTS OF SINGLE DROPLETS MOVING IN AN INFINITE DROPLET CHAIN ON THE AXIS OF A TUBE

D. Y. LIU,† K. ANDERS and A. FROHN

Institut für Thermodynamik der Luft- und Raumfahrt, Universität Stuttgart, Pfaffenwaldring 31, 7000 Stuttgart 80, B.R.D.

(*Received* 3 *June* 1986; *in revised form* 28 *September* 1987)

Abstract—The drag of monodisperse droplets moving in an infinite droplet chain is studied numerically and experimentally. The droplet chain produced by a vibrating orifice generator is composed of an infinite number of droplets with the same diameter σ_P and a constant spacing d_P. The droplets move with a velocity u_0 along the axis of a cylindrical tube of radius R. In the experiments the velocity decrease of the droplets is measured by a laser Doppler velocimeter. It is shown that near the wall the droplet chain produces the same flow field as a cylindrical rod with a diameter of $\sigma_P \exp(-f)$, where f is a function of the velocity u_0, the droplet diameter σ_P, the spacing of the droplets d_P and the radius of the tube R. With these assumptions the Navier–Stokes equations have been solved numerically. Drag coefficients c_D have been computed for Reynolds numbers from 20 to 100. The Reynolds number is based in this case on the droplet velocity u_0 and the droplet diameter σ_P. The dimensionless spacing d_P/σ_P was varied between 2 and 12 and the dimensionless tube diameter $2R/\sigma_P$ ranged from 20 to 1000. In addition, numerical results are presented for the radial coordinate δ of the boundary, at which the flow becomes essentially parallel to the tube, for the axial velocity at this boundary $u_z(z, \delta)$ and for the maximum value of the velocity along the axis of symmetry $u_z(z, 0)_{max}$. The results of the numerical calculations are compared with the experiments.

1. INTRODUCTION

For the theoretical description of multiphase flow the interaction between droplets and the surrounding gas is of great interest. The flow around single spheres has been treated in a number of different works (e.g. Stokes 1851; Oseen 1910; Rimon & Cheng 1969). The extension of the problem to two spheres has been treated, for instance, by Lee (1979), Tsuji *et al.* (1982) and by Pei & Hayward (1983). In the present paper the flow field of an infinite number of spheres moving along the centerline of a cylindrical tube is studied numerically. The drag coefficients obtained from these calculations have been compared with new experiments, which were performed with droplet chains of very high uniformity in droplet size and spacing. The droplet chains were produced with a vibrating orifice droplet generator, as described by Berglund & Liu (1973) and König *et al.* (1986). Such droplet systems provide precise and highly reproducible conditions for the investigation of droplet behavior. They may be used, for example, to study evaporation rates (Anders & Frohn 1984) or the interaction between droplets or between droplets and solid surfaces. Possible space applications of monodisperse droplet chains have been presented by Muntz *et al.* (1984). For the evaluation of experiments with droplet chains it is desirable to have a detailed knowledge of the flow field around the droplets.

2. BASIC EQUATIONS

A sequence of spheres with diameter σ_P is moving along the axis of a cylindrical tube of radius R. The spacing d_P between the droplets is constant. For these conditions one has an incompressible steady flow field with cylindrical symmetry and periodicity d_P in the axial direction. The continuity equation and the Navier–Stokes equations for the dimensionless velocity components $\bar{u}_r$ and $\bar{u}_z$ and the dimensionless pressure $\bar{p}$ may be written in cylindrical coordinates $(\bar{z}, \bar{r})$ as

$$\frac{\partial \bar{u}_z}{\partial \bar{z}} + \frac{\partial \bar{u}_r}{\partial \bar{r}} + \frac{\bar{u}_r}{\bar{r}} = 0, \qquad [1]$$

$$\bar{u}_z \frac{\partial \bar{u}_z}{\partial \bar{z}} + \bar{u}_r \frac{\partial \bar{u}_z}{\partial \bar{r}} = -\frac{\partial \bar{p}}{\partial \bar{z}} + \frac{2}{\mathrm{Re}}\left(\frac{\partial^2}{\partial \bar{z}^2} + \frac{\partial^2}{\partial \bar{r}^2} + \frac{1}{\bar{r}}\frac{\partial}{\partial \bar{r}}\right)\bar{u}_z, \qquad [2]$$

†Present address: Institute of Mechanics, Chinese Academy of Sciences, Beijing, People's Republic of China.

$$\bar{u}_z \frac{\partial \bar{u}_r}{\partial \bar{z}} + \bar{u}_r \frac{\partial \bar{u}_r}{\partial \bar{r}} = -\frac{\partial \bar{p}}{\partial \bar{r}} + \frac{2}{\mathrm{Re}}\left(\frac{\partial^2}{\partial \bar{z}^2} + \frac{\partial^2}{\partial \bar{r}^2} + \frac{1}{\bar{r}}\frac{\partial}{\partial \bar{r}} - \frac{1}{\bar{r}^2}\right)\bar{u}_r. \quad [3]$$

The problem is considered in a coordinate system in which the spheres are at rest and the tube is moving with velocity u_0, as shown in figure 1. The boundary conditions are

$$\bar{u}_z = 0 \quad \text{and} \quad \bar{u}_r = 0 \quad \text{at} \quad \bar{z}^2 + \bar{r}^2 = 1, \quad [4]$$

$$\frac{\partial \bar{u}_z}{\partial \bar{r}} = 0 \quad \text{and} \quad \bar{u}_r = 0 \quad \text{for} \quad \bar{r} = 0 \quad \text{and} \quad |\bar{z}| > 1, \quad [5]$$

$$\bar{u}_z\left(\bar{z} + \frac{d_\mathrm{P}}{\sigma_\mathrm{P}}, \bar{r}\right) = \bar{u}_z\left(\bar{z} - \frac{d_\mathrm{P}}{\sigma_\mathrm{P}}, \bar{r}\right) \quad [6]$$

$$\bar{u}_r\left(\bar{z} + \frac{d_\mathrm{P}}{\sigma_\mathrm{P}}, \bar{r}\right) = \bar{u}_r\left(\bar{z} - \frac{d_\mathrm{P}}{\sigma_\mathrm{P}}, \bar{r}\right) \quad [7]$$

$$\bar{u}_z = 1 \quad \text{at} \quad \bar{r} = \bar{R} \quad [8]$$

and

$$\bar{u}_r = 0 \quad \text{at} \quad \bar{r} = \bar{R}. \quad [9]$$

Using the density ρ and the kinematic viscosity ν the following dimensionless quantities have been introduced:

$$\bar{u}_z \equiv \frac{u_z}{u_0}, \quad \bar{u}_r \equiv \frac{u_r}{u_0}, \quad \bar{p} \equiv \frac{p}{(\rho u_0^2)}, \quad \bar{z} \equiv \frac{2z}{\sigma_\mathrm{P}}, \quad \bar{r} \equiv \frac{2r}{\sigma_\mathrm{P}}, \quad \bar{R} \equiv \frac{2R}{\sigma_\mathrm{P}}, \quad \mathrm{Re} \equiv \frac{u_0 \sigma_\mathrm{P}}{\nu}.$$

The dimensionless stream function $\bar{\psi}$ and the vorticity $\bar{\omega}$ are then given by

$$\mathrm{d}\bar{\psi} = \bar{r}\bar{u}_z\,\mathrm{d}\bar{r} - \bar{r}\bar{u}_r\,\mathrm{d}\bar{z} \quad \text{and} \quad \bar{\omega} = \frac{\partial \bar{u}_r}{\partial \bar{z}} - \frac{\partial \bar{u}_z}{\partial \bar{r}}.$$

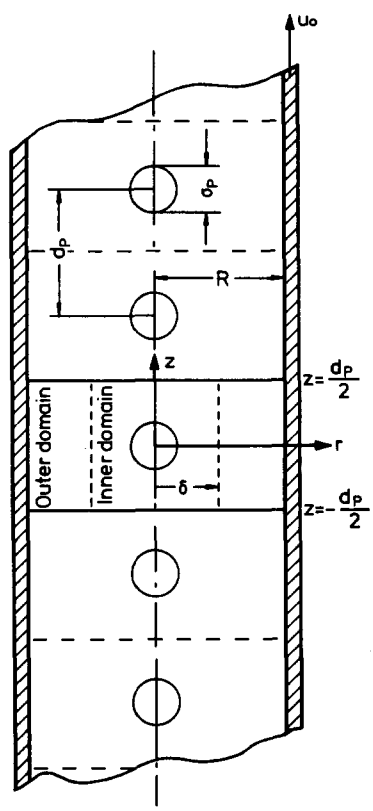

Figure 1. Geometry and coordinates.

Due to the boundary conditions the flow field may be divided into two regions. One region, which is called the inner domain, in which the flow field is strongly influenced by the presence of the spheres and another region close to the wall, in which the flow is essentially parallel to the axis. This region is called the outer domain. The actual position of the boundary between both regions is unknown *a priori*. In the outer domain one has

$$\bar{u}_r = 0, \quad \frac{\partial \bar{u}_z}{\partial \bar{z}} = 0 \quad \text{and} \quad \frac{\partial \bar{p}}{\partial \bar{z}} = 0.$$

Equation [2] can therefore be written as

$$\frac{\partial^2 \bar{u}_z}{\partial \bar{r}^2} + \frac{1}{\bar{r}} \frac{\partial \bar{u}_z}{\partial \bar{r}} = 0.$$

From this equation and the boundary condition [8], one gets for the outer domain the solution

$$\bar{u}_z(\bar{z}, \bar{r}) = 1 - \bar{A}(\ln \bar{R} - \ln \bar{r}) \qquad [10]$$

with the constant

$$\bar{A} = \left(\bar{r} \frac{\partial \bar{u}_z}{\partial \bar{r}} \right)_{\text{outer domain}}. \qquad [11]$$

For the case where the droplet chain is replaced by a cylindrical rod with diameter σ_P one would get

$$\bar{A} = \frac{1}{\ln \bar{R}}. \qquad [12]$$

For the inner domain the continuity equation and the Navier–Stokes equations [1]–[3] have to be solved numerically. The boundary conditions [4]–[7] are still valid, the boundary conditions [8] and [9] on the inner surface of the tube however have to be replaced by new boundary conditions at the boundary between the inner and outer domain. Here one has

$$\bar{r} \frac{\partial \bar{u}_z}{\partial \bar{r}} = \bar{A} \quad \text{at} \quad \bar{r} \geqslant \bar{\delta} \qquad [13]$$

and

$$\bar{u}_r = 0 \quad \text{at} \quad \bar{r} \geqslant \bar{\delta}, \qquad [14]$$

where $\bar{\delta} = 2\delta/\sigma_P$ is the dimensionless radial coordinate for the boundary between the inner and outer domain. The conditions [13] and [14] are also valid throughout the whole outer domain. As the actual position of this boundary is not known *a priori*, the numerical calculation has to be performed in the whole inner domain and in part of the outer domain.

In the system [1]–[9] one has three dimensionless parameters. By introduction of the following new dimensionless quantities,

$$\left.\begin{aligned}
\tilde{u}_z &\equiv \frac{\bar{u}_z}{\bar{A}}, \\
\tilde{u}_r &\equiv \frac{\bar{u}_r}{\bar{A}}, \\
\tilde{p} &\equiv \frac{\bar{p}}{\bar{A}^2}, \\
\tilde{r} &\equiv \bar{r}, \\
\tilde{z} &\equiv \bar{z}, \\
\widetilde{\mathrm{Re}} &\equiv \bar{A} \cdot \widetilde{\mathrm{Re}}, \\
\mathrm{d}\tilde{\psi} &\equiv \tilde{r}\tilde{u}_z \,\mathrm{d}\tilde{r} - \tilde{r}\tilde{u}_r \,\mathrm{d}\tilde{z} = \frac{\mathrm{d}\bar{\psi}}{\bar{A}}, \\
\tilde{\omega} &\equiv \frac{\partial \tilde{u}_r}{\partial \tilde{z}} - \frac{\partial \tilde{u}_z}{\partial \tilde{r}} = \frac{\bar{\omega}}{\bar{A}},
\end{aligned}\right\} \qquad [15]$$

the problem is reduced to a system with two parameters. Hence the dimensionless continuity equation and the Navier–Stokes equations are given by

$$\frac{\partial \tilde{u}_z}{\partial \tilde{z}} + \frac{\partial \tilde{u}_r}{\partial \tilde{r}} + \frac{\tilde{u}_r}{\tilde{r}} = 0, \tag{16}$$

$$\tilde{u}_z \frac{\partial \tilde{u}_z}{\partial \tilde{z}} + \tilde{u}_r \frac{\partial \tilde{u}_z}{\partial \tilde{r}} = -\frac{\partial \tilde{p}}{\partial \tilde{z}} + \frac{2}{\widetilde{\mathrm{Re}}}\left(\frac{\partial^2}{\partial \tilde{z}^2} + \frac{\partial^2}{\partial \tilde{r}^2} + \frac{1}{\tilde{r}}\frac{\partial}{\partial \tilde{r}}\right)\tilde{u}_z, \tag{17}$$

$$\tilde{u}_z \frac{\partial \tilde{u}_r}{\partial \tilde{z}} + \tilde{u}_r \frac{\partial \tilde{u}_r}{\partial \tilde{r}} = -\frac{\partial \tilde{p}}{\partial \tilde{r}} + \frac{2}{\widetilde{\mathrm{Re}}}\left(\frac{\partial^2}{\partial \tilde{z}^2} + \frac{\partial^2}{\partial \tilde{r}^2} + \frac{1}{\tilde{r}}\frac{\partial}{\partial \tilde{r}} - \frac{1}{\tilde{r}^2}\right)\tilde{u}_r; \tag{18}$$

with the boundary conditions

$$\tilde{u}_z = 0, \quad \tilde{u}_r = 0 \quad \text{at} \quad \tilde{z}^2 + \tilde{r}^2 = 1, \tag{19}$$

$$\frac{\partial \tilde{u}_z}{\partial \tilde{r}} = 0, \quad \tilde{u}_r = 0 \quad \text{for} \quad \tilde{r} = 0, \quad |\tilde{z}| > 1, \tag{20}$$

$$\tilde{u}_z\left(\tilde{z} + \frac{d_\mathrm{P}}{\sigma_\mathrm{P}}, r\right) = \tilde{u}_z\left(\tilde{z} - \frac{d_\mathrm{P}}{\sigma_\mathrm{P}}, \tilde{r}\right) \tag{21}$$

$$\tilde{u}_r\left(\tilde{z} + \frac{d_\mathrm{P}}{\sigma_\mathrm{P}}, r\right) = \tilde{u}_r\left(\tilde{z} - \frac{d_\mathrm{P}}{\sigma_\mathrm{P}}, \tilde{r}\right) \tag{22}$$

and

$$\tilde{r}\frac{\partial \tilde{u}_z}{\partial \tilde{r}} = 1, \quad \tilde{u}_r = 0 \quad \text{at} \quad \tilde{r} \geqslant \bar{\delta}. \tag{23}$$

The solutions of these equations are governed by only two independent parameters, namely by $\widetilde{\mathrm{Re}}$ and $d_\mathrm{P}/\sigma_\mathrm{P}$, instead of three parameters as in the system [1]–[3], with the boundary conditions [4]–[7], [13] and [14]. Thus, each quantity is a function of these two parameters. For the extension of the inner domain one gets

$$\tilde{\delta} = F_1\left(\frac{d_\mathrm{P}}{\sigma_\mathrm{P}}, \widetilde{\mathrm{Re}}\right). \tag{24}$$

The velocity at this boundary can be written as

$$\tilde{u}_z(\tilde{z}, \tilde{\delta}) = F_2\left(\frac{d_\mathrm{P}}{\sigma_\mathrm{P}}, \widetilde{\mathrm{Re}}\right). \tag{25}$$

The maximum of the velocity on the axis of symmetry,

$$\tilde{u}_z(\tilde{z}, 0)_{\max} = F_3\left(\frac{d_\mathrm{P}}{\sigma_\mathrm{P}}, \widetilde{\mathrm{Re}}\right), \tag{26}$$

and the drag coefficient,

$$\tilde{c}_\mathrm{D} = \frac{D}{\frac{\pi}{8}\rho \mathrm{A}^2 \sigma_\mathrm{P}^2} = F_4\left(\frac{d_\mathrm{P}}{\sigma_\mathrm{P}}, \widetilde{\mathrm{Re}}\right), \tag{27}$$

are also functions of these dimensionless parameters. The quantity

$$\mathrm{A} = \left(r\frac{\partial u_z}{\partial r}\right)_{r>\delta} = \bar{\mathrm{A}} u_0 \tag{28}$$

is a characteristic velocity and the drag D is defined by

$$D = \left(2\pi r d_\mathrm{P} \mu \frac{\partial u_z}{\partial r}\right)_{r>\delta}, \tag{29}$$

where μ is the dynamic viscosity. From [27]–[29] it follows that

$$F_4 = \frac{16}{\widetilde{\mathrm{Re}}} \frac{d_\mathrm{P}}{\sigma_\mathrm{P}}. \qquad [30]$$

The functions F_1, F_2 and F_3 have to be determined numerically.

3. NUMERICAL CALCULATIONS

For the numerical calculations the stream function $\bar{\psi}$ and the quantity $\bar{\zeta} = \bar{\omega}/\bar{r}$ have been introduced. It follows that

$$\bar{\rho}^2 \sin^2\theta \left[\frac{\partial}{\partial\bar{\rho}}\left(\bar{\zeta}\frac{\partial\bar{\psi}}{\partial\theta}\right) - \frac{\partial}{\partial\theta}\left(\bar{\zeta}\frac{\partial\bar{\psi}}{\partial\bar{\rho}}\right)\right] = \frac{2}{\mathrm{Re}}\frac{\partial}{\partial\bar{\rho}}\left(\bar{\rho}^4 \sin^3\theta \frac{\partial\bar{\zeta}}{\partial\bar{\rho}}\right) + \frac{2}{\mathrm{Re}}\frac{\partial}{\partial\theta}\left(\bar{\rho}^2 \sin^3\theta \frac{\partial\bar{\zeta}}{\partial\theta}\right) \qquad [31]$$

and

$$\frac{\partial}{\partial\bar{\rho}}\left(\frac{1}{\sin\theta}\frac{\partial\bar{\psi}}{\partial\bar{\rho}}\right) + \frac{\partial}{\partial\theta}\left(\frac{1}{\bar{\rho}^2\sin\theta}\frac{\partial\bar{\psi}}{\partial\theta}\right) + \bar{\rho}^2 \sin\theta \cdot \bar{\zeta} = 0. \qquad [32]$$

Here the spherical coordinates $(\bar{\rho}, \theta, \phi)$ have been used, where $\bar{\rho} = (\bar{r}^2 + \bar{z}^2)^{1/2}$ is the dimensionless radial coordinate. The boundary conditions can be written as

$$\bar{\psi} = 0 \quad \text{and} \quad \frac{\partial\bar{\zeta}}{\partial\theta} = 0 \quad \text{at} \quad \theta = 0 \quad \text{or} \quad \theta = \pi,$$

$$\bar{\psi} = 0 \quad \text{and} \quad \frac{\partial\bar{\psi}}{\partial\bar{\rho}} = 0 \quad \text{at} \quad \bar{\rho} = 1,$$

$$\bar{\psi} = \bar{\psi}_\mathrm{M} \quad \text{and} \quad \left(\sin\theta\frac{\partial}{\partial\bar{\rho}} + \frac{\cos\theta}{\bar{\rho}}\frac{\partial}{\partial\theta}\right)(\bar{\zeta}\bar{\rho}^2\sin^2\theta) = 0 \quad \text{at} \quad \bar{\rho}\sin\theta = \bar{r}_\mathrm{M},$$

$$\bar{\psi}\left(\sqrt{\left(\bar{z} + \frac{d_\mathrm{P}}{\sigma_\mathrm{P}}\right)^2 + \bar{r}^2}, \arctan\left(\frac{\bar{r}}{\bar{z} + \frac{d_\mathrm{P}}{\sigma_\mathrm{P}}}\right)\right) = \bar{\psi}\left(\sqrt{\left(\bar{z} - \frac{d_\mathrm{P}}{\sigma_\mathrm{P}}\right)^2 + \bar{r}^2}, \pi - \arctan\left(\frac{\bar{r}}{\bar{z} - \frac{d_\mathrm{P}}{\sigma_\mathrm{P}}}\right)\right)$$

and

$$\bar{\zeta}\left(\sqrt{\left(\bar{z} + \frac{d_\mathrm{P}}{\sigma_\mathrm{P}}\right)^2 + \bar{r}^2}, \arctan\left(\frac{\bar{r}}{\bar{z} + \frac{d_\mathrm{P}}{\sigma_\mathrm{P}}}\right)\right) = \bar{\zeta}\left(\sqrt{\left(\bar{z} - \frac{d_\mathrm{P}}{\sigma_\mathrm{P}}\right)^2 + \bar{r}^2}, \pi - \arctan\left(\frac{\bar{r}}{\bar{z} - \frac{d_\mathrm{P}}{\sigma_\mathrm{P}}}\right)\right).$$

For the numerical calculations the outer radius $\bar{r}_\mathrm{M}$ of the domain of calculation and the corresponding value of the stream function $\bar{\psi}_\mathrm{M}$ have to be chosen. This radius $\bar{r}_\mathrm{M}$ has to be outside of the inner domain, this means the numerical calculations are performed in the whole inner domain plus part of the outer domain. This is necessary to determine the *a priori* unknown value of the radial coordinate $\bar{\delta}$ of the boundary between the inner and outer domain. The values for $\bar{\psi}$, $\bar{u}_z(\bar{z}, \bar{\delta})$ and $\bar{u}_z(\bar{z}, 0)_{\max}$ are obtained from the results of the numerical calculations for $\bar{\psi}$, $\bar{u}_z(\bar{z}, \bar{\delta})$ and $\bar{u}_z(\bar{z}, 0)_{\max}$ by division of these values by $\bar{\mathrm{A}} = [-\bar{\zeta}\bar{r}^2]_{\bar{r}=\bar{r}_\mathrm{M}}$. The Reynolds number $\widetilde{\mathrm{Re}}$ is given by

$$\widetilde{\mathrm{Re}} = \mathrm{Re} \cdot \bar{\mathrm{A}}.$$

The natural logarithm of the dimensionless radius

$$s = \ln\bar{\rho}$$

was introduced, in order to get in the $\bar{\rho}$–θ plane a grid with narrow meshes close to the surface

of the sphere. The derivatives are given by

$$\frac{\partial}{\partial \bar{\rho}} = e^{-s}\frac{\partial}{\partial s} \quad \text{and} \quad \frac{\partial^2}{\partial \bar{\rho}^2} = e^{-2s}\left(\frac{\partial^2}{\partial s^2} - \frac{\partial}{\partial s}\right).$$

According to Roache (1976) and Gosman *et al.* (1969) the corresponding difference equation can be written as

$$\bar{\psi}_{i,j} = \frac{c_E\bar{\psi}_{i+1,j} + c_W\bar{\psi}_{i-1,j} + c_N\bar{\psi}_{i,j+1} + c_S\bar{\psi}_{i,j-1} + \exp(4s)\bar{\zeta}_{i,j}}{c_E + c_W + c_N + c_S}$$

and

$$\bar{\zeta}_{i,j} = \frac{\begin{aligned}&[(A_E + B_E\exp(s_i))\bar{\zeta}_{i+1,j} + (A_W + B_W\exp(s_i))\bar{\zeta}_{i-1,j}\\ &+ (A_N + B_N\exp(s_i))\zeta_{i,j+1} + (A_S + B_S\exp(s_i))\bar{\zeta}_{i,j-1}]\end{aligned}}{[(A_E + A_W + A_N + A_S) + (B_E + B_W + B_N + B_S)\exp(s_i)]}.$$

Here the following abbreviations have been used:

$$c_E = \frac{e^{-0.5\Delta s}}{\Delta s^2 \sin^2\theta_j},$$

$$c_W = \frac{e^{+0.5\Delta s}}{\Delta s^2 \sin^2\theta_j},$$

$$c_N = \frac{1}{\Delta\theta^2 \sin\theta_j \sin(\theta_j + 0.5\Delta\theta)},$$

$$c_S = \frac{1}{\Delta\theta^2 \sin\theta_j \sin(\theta_j - 0.5\Delta\theta)},$$

$$B_E = \frac{16}{Re}\sin\theta_j e^{1.5\Delta s}\frac{\Delta\theta}{\Delta s},$$

$$B_W = \frac{16}{Re}\sin\theta_j e^{-1.5\Delta s}\frac{\Delta\theta}{\Delta s},$$

$$B_N = \frac{16}{Re}\frac{\sin^3(\theta_j + 0.5\Delta\theta)}{\sin^2\theta_j}\frac{\Delta s}{\Delta\theta},$$

$$B_S = \frac{16}{Re}\frac{\sin^3(\theta_j - 0.5\Delta\theta)}{\sin^2\theta_j}\frac{\Delta s}{\Delta\theta},$$

$$A_E = (\bar{\psi}_{i+1,j-1} + \bar{\psi}_{i,j-1} - \bar{\psi}_{i+1,j+1} - \bar{\psi}_{i,j+1}),$$

$$A_W = (\bar{\psi}_{i-1,j+1} + \bar{\psi}_{i,j+1} - \bar{\psi}_{i-1,j-1} - \bar{\psi}_{i,j-1}),$$

$$A_N = (\bar{\psi}_{i+1,j+1} + \bar{\psi}_{i+1,j} - \bar{\psi}_{i-1,j+1} - \bar{\psi}_{i-1,j})$$

and

$$A_S = (\bar{\psi}_{i-1,j-1} + \bar{\psi}_{i-1,j} - \bar{\psi}_{i+1,j-1} - \bar{\psi}_{i+1,j}).$$

The domain of calculation is bounded in the $\bar{r}$-direction by $\bar{r} = 0$ and $\bar{r} = \bar{r}_M$, and in the $\bar{z}$-direction by $\bar{z} = -(d_P/\sigma_P)$ and $\bar{z} = +(d_P/\sigma_P)$. The calculations are performed in spherical coordinates, therefore the values along these straight boundaries have to be calculated from values at nodes inside the domain of calculation. This means, for example, that the values at the upper bound $\bar{z} = +(d_P/\sigma_P)$ are interpolated from values inside the domain of calculation and values outside the domain of calculation. The latter can be calculated due to the periodicity of the problem from values inside the domain at the lower bound $\bar{z} = -(d_P/\sigma_P)$. Along the upper and lower

boundary at $z = \pm(d_P/\sigma_P)$ the quantities $\bar{\psi}$ and $\bar{\zeta}$ have been expressed as linear functions in $\bar{z}$ by

$$\frac{\bar{\psi}}{\bar{r}^2} = f_1(\bar{r}^2) + f_2(\bar{r}^2)\left(\bar{z} \mp \frac{d_P}{\sigma_P}\right)$$

and

$$\bar{\zeta} = f_3(\bar{r}^2) + f_4(\bar{r}^2)\left(\bar{z} \mp \frac{d_P}{\sigma_P}\right).$$

The functions

$$f_i(\bar{r}^2) = f_i(\chi) = \sum_{j=1}^{n} v_{i,j}\Delta_{j-4}(\chi), \quad i = 1, 2, 3, 4, n = 8$$

are third-order spline functions [as described, for instance, by Feng (1978), Curry & Schoenberg (1966) and deBoor (1978)] with coefficients $v_{i,j}$ which have been determined by the least-squares method. Here the following abbreviations have been used:

$$\Delta_s(\chi) \equiv \frac{1}{2}\sum_{p=s}^{s+4} \beta_{s,p}|\chi - \chi_p|^3, \quad s = -3, -2, -1, \ldots, n-4,$$

$$\beta_{s,p} \equiv \frac{4!}{\Omega_s(\chi_p)}$$

and

$$\Omega_s(\chi_p) \equiv \prod_{\substack{k=s \\ k\neq p}}^{s+4} (\chi_p - \chi_k).$$

The upper and lower boundary was divided into n sections. The radial coordinates of the nodes of intersection are denoted by $\bar{r}_k$. Along the boundary $\bar{r} = \bar{r}_M$ a linear extrapolation from values inside the domain of calculation was sufficient.

4. NUMERICAL RESULTS

The results of these calculations are shown in figures 2–4, where the quantities $\tilde{\delta}, \tilde{u}_z(\tilde{z}, \tilde{\delta})$ and $\tilde{u}_z(\tilde{z}, 0)_{max}$ are plotted against the Reynolds number $\widetilde{Re}$ for different dimensionless spacings d_P/σ_P.

As the variation of the flow quantities at the boundary between the inner and outer domain is continuous and smooth one has to define the location of this boundary. In analogy to the definitions of boundary layer thickness introduced in boundary layer theory a quantity

$$\alpha(\tilde{r}) = \frac{((\tilde{r}\tilde{\omega})_{max} - (\tilde{r}\tilde{\omega})_{min})}{(\tilde{r}\tilde{\omega})_{av}} \qquad [33]$$

is used. The boundary between the outer and inner domain is then defined by $\tilde{r} = \text{const}$, where

$$\alpha(\tilde{r}) = 0.05.$$

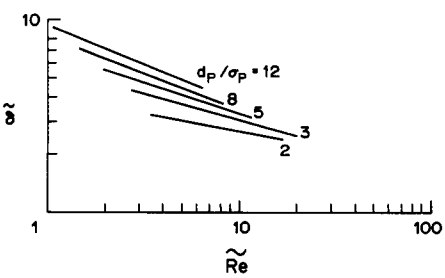

Figure 2. Extension of $\tilde{\delta}$ of the innner domain as a function of droplet spacing d_P/σ_P and Reynolds number $\widetilde{Re}$.

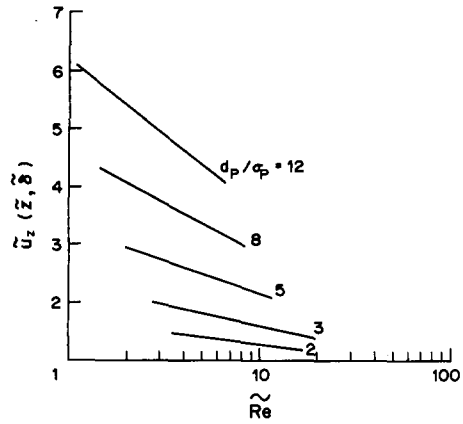

Figure 3. Velocity component $\tilde{u}_z$ at the boundary between the inner and outer domain as a function of droplet spacing d_P/σ_P and Reynolds number $\widetilde{Re}$.

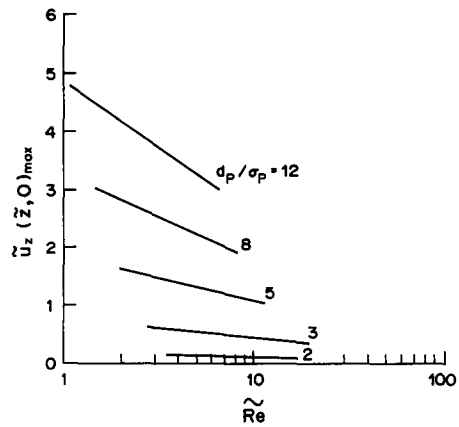

Figure 4. Maximum value of the velocity component $\tilde{u}_z$ along the axis of the cylinder as a function of droplet spacing d_P/σ_P and Reynolds number $\widetilde{Re}$.

Usually velocities are used to define a boundary layer thickness. The velocity components are obtained by differentiation of the stream function $\bar{\psi}$. As the numerical error is increased by this procedure the quantity $\tilde{r}\tilde{\omega}$, instead of the velocity components $\tilde{u}_z$ and $\tilde{u}_r$, was used for the definition of the boundary between the inner and outer domain. In figure 5 some typical $\tilde{r}\tilde{\omega}$-distributions are plotted over $\tilde{z}$ for three different radii. One can see that the for increasing values of $\tilde{r}$ the value $(\tilde{r}\tilde{\omega})_{max}$ decreases and the value $(\tilde{r}\tilde{\omega})_{min}$ increases, whereas the average value

$$(\tilde{r}\tilde{\omega})_{av} = \frac{\sigma_P}{2d_P}\int_{-(d_P/\sigma_P)}^{+(d_P/\sigma_P)} (\tilde{r}\tilde{\omega})\,d\tilde{z}$$

is almost constant. Furthermore, it can be shown that along the line $\tilde{r} = 1$,

$$(\tilde{r}\tilde{\omega})_{min} \approx 0 \quad \text{and} \quad (\tilde{r}\tilde{\omega})_{max} \approx \frac{d_P}{\sigma_P}.$$

Thus, one gets

$$\alpha(1) \approx \frac{d_P}{\sigma_P}.$$

The entire flow field is determined when the quantity $\bar{A}$ is known. Replacing $\bar{r}$ by $\tilde{\delta}$ in [10], one gets

$$\bar{A} = \frac{1}{\ln \bar{R} + f\left(\dfrac{d_P}{\sigma_P}, \bar{A}\cdot Re\right)}, \qquad [34]$$

where the function f is given by

$$f\left(\frac{d_P}{\sigma_P}, \widetilde{Re}\right) = F_2\left(\frac{d_P}{\sigma_P}, \widetilde{Re}\right) - \ln\left[F_1\left(\frac{d_P}{\sigma_P}, \widetilde{Re}\right)\right]. \qquad [35]$$

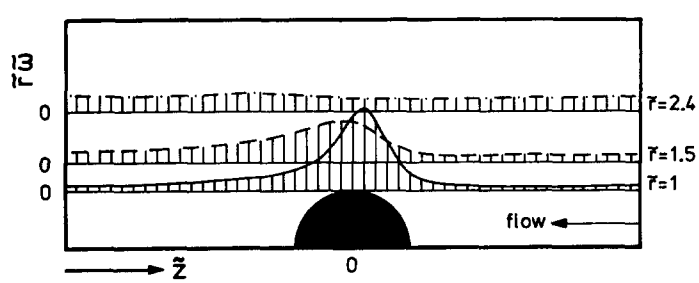

Figure 5. Typical distribution of the quantity $\tilde{r}\tilde{\omega}$ in the $\tilde{z}$-direction for different radii $\tilde{r}$. This quantity is used to define the boundary between the inner and outer domain.

The quantity $\bar{A}$ and the function f are plotted in figures 6 and 7. Comparing [12] and [34] one realizes that a droplet chain consisting of droplets with diameter σ_P produces the same flow field in the outer domain as a cylindrical rod with a diameter $\sigma_P \cdot \exp(-f)$.

From the numerical calculations one obtains the velocity distribution around the sphere. One can calculate the drag coefficient either using [30] or by integrating the pressure and shear stress resulting from the velocity distribution along the surface of the sphere. The difference between both methods was in all cases <4%. This deviation was obviously determined by the accuracy of the numerical calculations.

A typical velocity plot obtained via the numerical calculations is shown as a vector plot in figure 8. The corresponding velocities in the axial direction $\tilde{u}_z$ are plotted in figure 9 for different radial coordinates for the periodicity interval $-d_P/\sigma_P < z < d_P/\sigma_P$. The coordinate $\tilde{r} = 2r/\sigma_P$ is measured from the centerline of the cylindrical tube, as indicated in figure 1.

The drag coefficient of a sphere is usually defined as

$$c_D = \frac{D}{\frac{\pi}{8}\rho u_0^2 \sigma_P^2}.$$

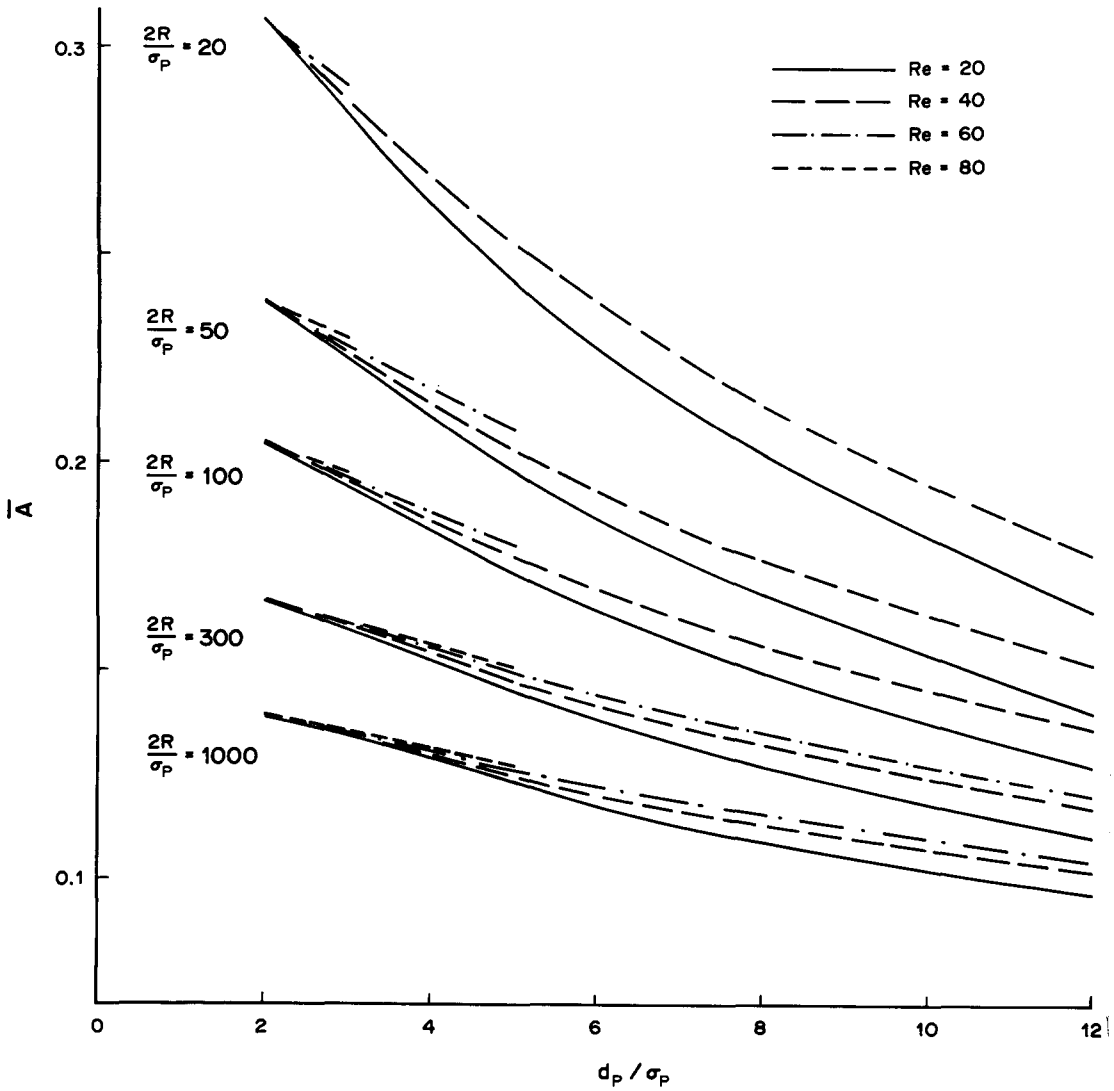

Figure 6. Quantity $\bar{A} = \tilde{r}(\partial \tilde{u}_z/\partial \tilde{r})_{\text{outer domain}}$ as a function of droplet spacing d_P/σ_P and Reynolds number Re.

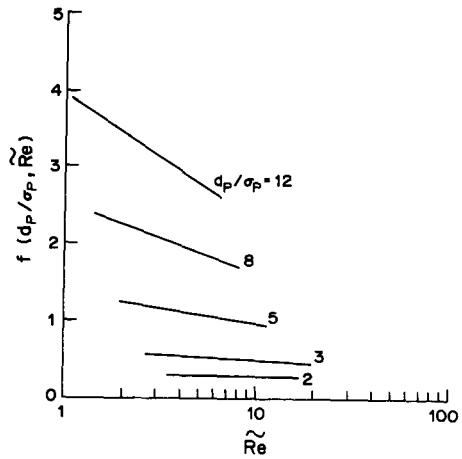

Figure 7. Function f introduced in [34] as a function of droplet spacing d_P/σ_P and Reynolds number $\tilde{Re}$.

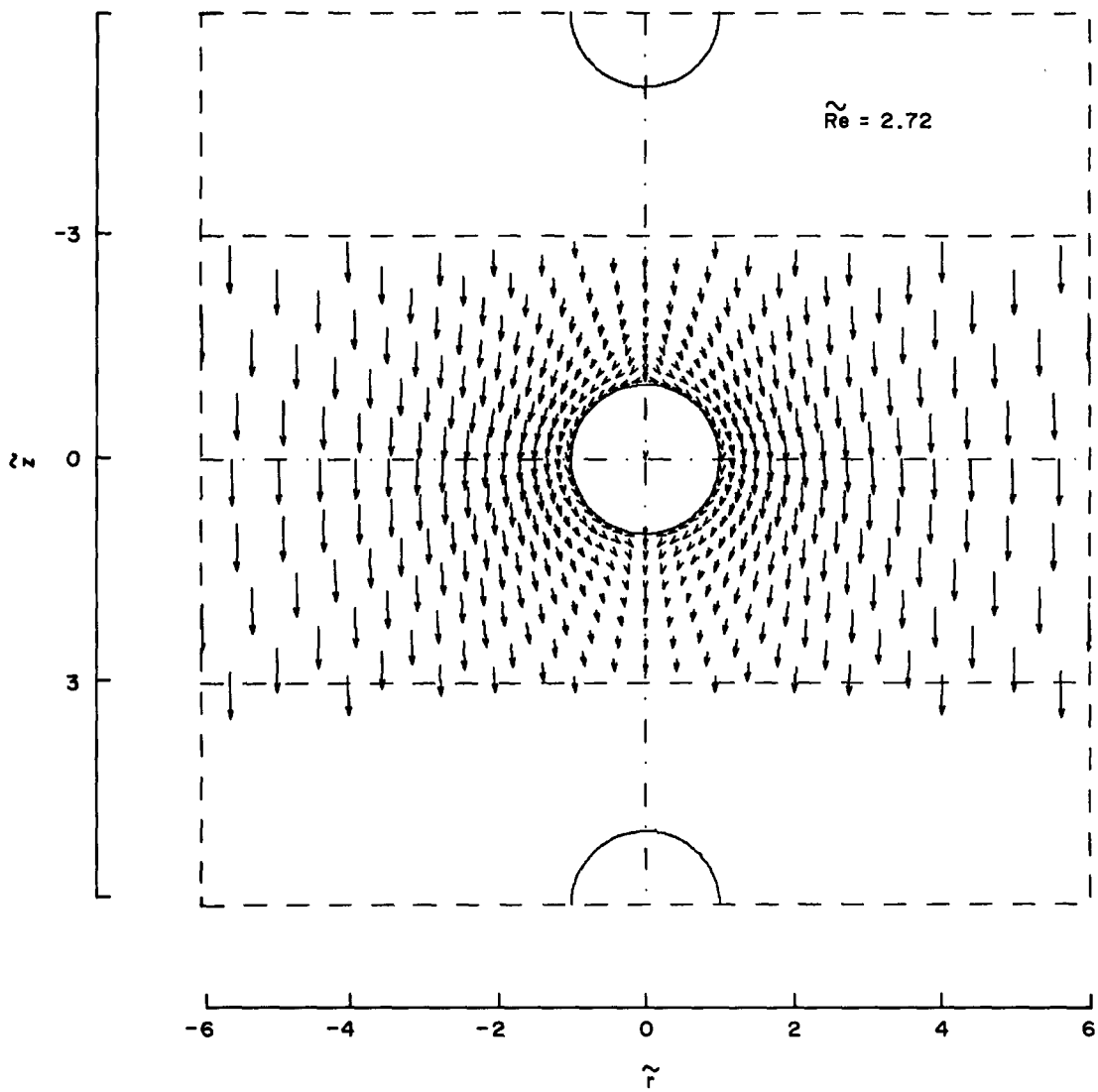

Figure 8. Typical vector plot of the velocity in the periodicity interval $-3 < \tilde{z} < 3$. In the $\tilde{r}$-direction the domain of calculation is bounded by $\tilde{r} = \tilde{r}_M = 6$.

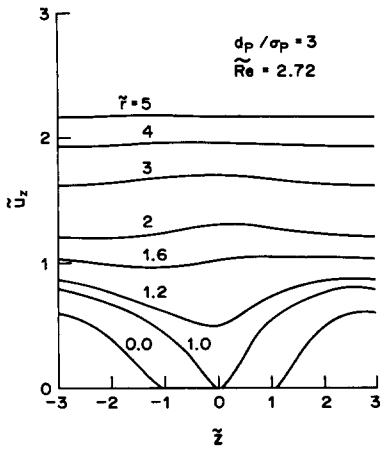

Figure 9. Velocity component $\tilde{u}_z$ in the periodicity interval $-3 < \tilde{z} < 3$ for different radii $\tilde{r}$.

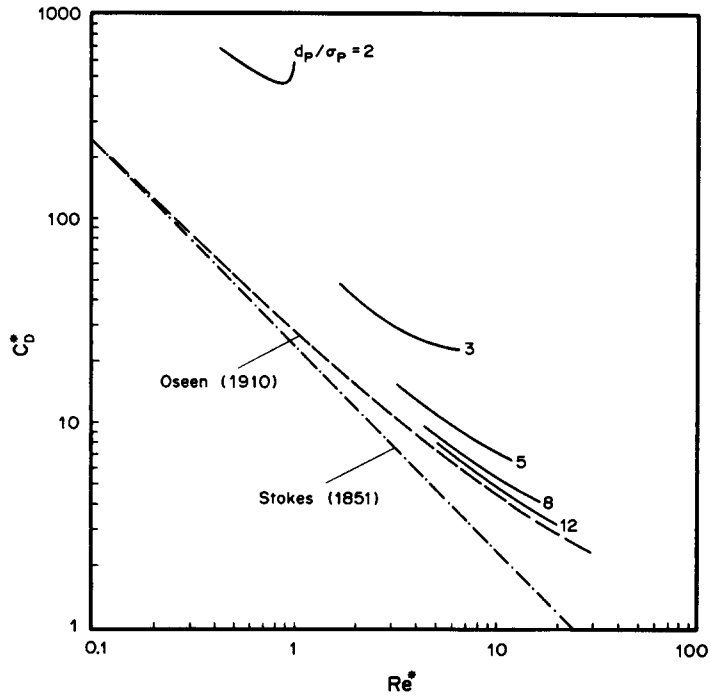

Figure 10. Comparison of the drag coefficient of single droplets in an undisturbed parallel free stream with the drag coefficient of a droplet in an infinite chain. For the calculation of c_D^* and Re* the velocity $U = u_z(z, 0)_{max}$ was used.

Using [28] and [29] the drag coefficient can be written as

$$c_D = \frac{16}{\mathrm{Re}} \frac{d_P}{\sigma_P} \bar{A}. \qquad [36]$$

In order to compare the results of the numerical calculations with results for single spheres a new definition of the drag coefficient

$$c_D^* = \frac{D}{\frac{\pi}{8} \rho U^2 \sigma_P^2}$$

is introduced, where

$$U = u_z(z, 0)_{max}$$

is the maximum of the velocity along the axis of symmetry. The corresponding Reynolds number is defined by

$$\mathrm{Re}^* = \frac{U \sigma_P}{\nu}.$$

In the case of an infinite chain of spheres, each sphere is moving in a flow field influenced by the preceeding sphere. In this flow field the velocities are in general not parallel to the axis and not constant along the radial coordinate. Therefore a direct comparison of the drag coefficient of a single sphere in a parallel flow and the drag coefficient of a sphere in an infinite droplet chain is not possible. However, for increasing values of d_P/σ_P the drag coefficient c_D^* should approach the drag coefficient of a single sphere. This is confirmed by the results plotted in figure 10.

5. EXPERIMENTS

The theoretical results of the present paper have been compared with new experimental results obtained via measurement of the velocity of monodisperse droplets moving in a glass tube. The

droplets were generated using a vibrating orifice droplet generator, which is shown schematically in figure 11. Liquid is forced through a small orifice with a constant feed rate $\dot{V}$. By appropriate choice of the driving pressure difference, which determines the feed rate, one obtains a laminar jet. This jet is excited by a piezoceramic disk with a frequency f_G. Within a certain range of excitation frequencies the laminar jet disintegrates into a monodisperse droplet chain of very high uniformity. The droplets all have the same diameter σ_P and the same spacing d_P. The droplet diameter is given by

$$\sigma_P = \left(\frac{6\dot{V}}{\pi f_G}\right)^{1/3}. \quad [37]$$

This relation results from the conservation of mass. In the experiments the droplet diameter was measured using a new light scattering technique, which evaluates the intensity distribution of the light scattered by the droplets. This technique has been described in more detail by König *et al.* (1986). With this technique the droplet diameter could be determined with an accuracy of 2%.

The average velocity of the liquid jet within the orifice,

$$u_j = \frac{4\dot{V}}{\pi d_G^2}, \quad [38]$$

is approximately equal to the velocity of the droplets u_0, if one neglects expansion or contraction of the jet as well as any change in momentum due to the disintegration of the jet or the influence of external forces. Here d_G is the diameter of the orifice. The spacing between the droplets d_P is a function of the frequency of excitation, the liquid feed rate and the orifice diameter. It is given by

$$d_P = \frac{u_0}{f_G}. \quad [39]$$

A photograph of the droplet chain and the cylindrical tube is shown in figure 12. Due to the drag, the droplet velocity decreases along the axis of the tube. Therefore the droplet spacing decreases slightly. The variation in the value of d_P from droplet to droplet is $<0.1\%$. For droplet velocities of approx. 10 m/s, used in the experiments of the present paper, the maximum velocity in the flow field between the droplets is in the range of 1–2 m/s. If one uses this value for a rough estimate of the Reynolds number one obtains for droplets with diameters of 100 μm Reynolds numbers of the order of 10. This means that there is no region, or only a very small one, of recirculating flow. The high uniformity of the droplet stream is maintained within a certain distance from the orifice. Therefore, the measurements can be performed only within a finite distance from the generator.

The experimental setup for the determination of the droplet velocities is shown schematically in figure 13. The droplet chain produced by the droplet generator DG moves along the axis of a cylindrical tube of glass with radius R. At different distances x along the axis the droplet velocity u_0 is measured with a laser Doppler velocimeter. The laser beam is split with a prism P. Both beams are brought into focus at the centerline of the tube by lens L1. At this point the probe volume is formed by the intersection of both beams. The intensity of one beam is registered by the photodiode D1, whereas the other beam is trapped by a beam stop BS. The Doppler signal of single droplets is collected by lens L2 and registered by the photodiode D2. As long as the droplet chain is monodisperse and regular one obtains from these two detectors periodical output signals, as shown in figure 14. The signal of photodiode D1 is used to survey the uniformity of the droplet chain. Only for a monodisperse droplet chain with constant droplet spacing is a periodic signal obtained.

The velocity of the droplets can be determined from the Doppler signal using the relation

$$u_0 = \frac{\lambda_L (n-1)}{2 \sin \frac{\gamma}{2} \cdot t_P}, \quad [40]$$

where λ_L is the wavelength of the laser light, γ is the angle of intersection of the two laser beams and t_P is the time elapsed between n successive maxima or minima in the Doppler signal. The droplet velocity at a certain distance x has been determined by evaluating up to 15 successive

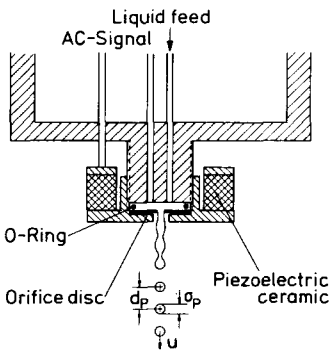

Figure 11. Schematic view of the droplet generator.

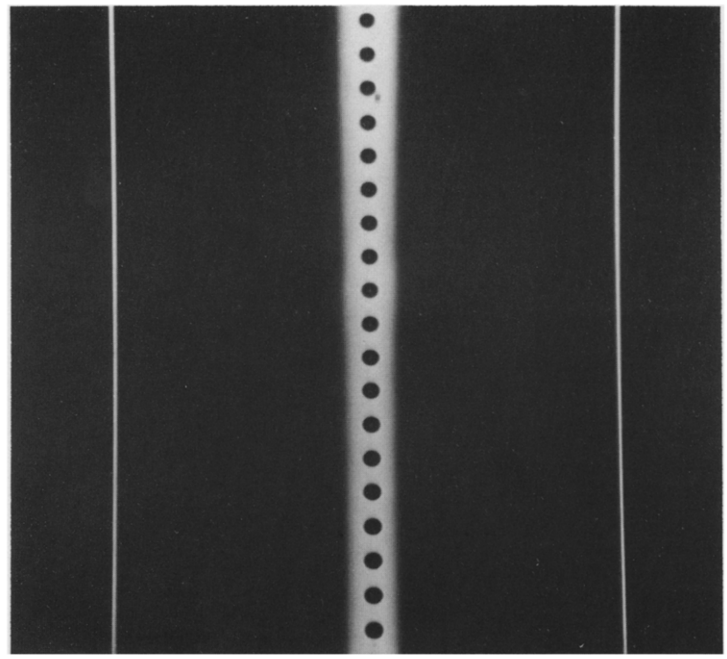

Figure 12. Photograph of a monodisperse droplet chain on the centerline of a glass tube.

Doppler signals recorded on a transient recorder. The dimensions of the probe volume have to be chosen in such a way that at any time only one droplet is within the probe volume of the laser Doppler velocimeter. Equations [38] and [39] were used to check the measured droplet diameters and velocities.

Some experimental results are plotted in figures 15–17. In the experiments the velocity of the droplets was measured at different locations along the axis of the tube. The comparison of the numerical calculations with these experimentally determined velocity variations is shown in figures 15 and 16. For these calculations it has been assumed that the drag coefficient is constant within intervals of 0.5 mm along the axis. The dashed lines in figures 15 and 16 show the velocity of a single droplet with the same initial conditions in an unconfined flow field. In figure 15 the measurements and the theoretical predictions for four different initial velocities are plotted. The droplet diameter σ_P and dimensionless spacing d_P/σ_P are practically constant for this figure. The influence of the droplet diameter is shown in figure 16. Here the initial droplet velocity u_0 and the dimensionless droplet spacing d_P/σ_P are kept constant. The agreement between the experimental results and the theoretical predictions is very good. For larger droplet velocities a small deviation

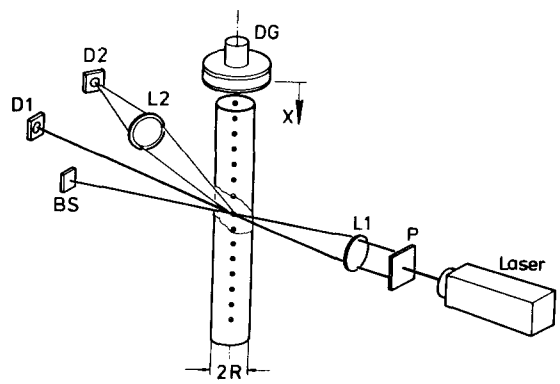

Figure 13. Experimental setup for velocity measurements. The abbreviations are explained in the text.

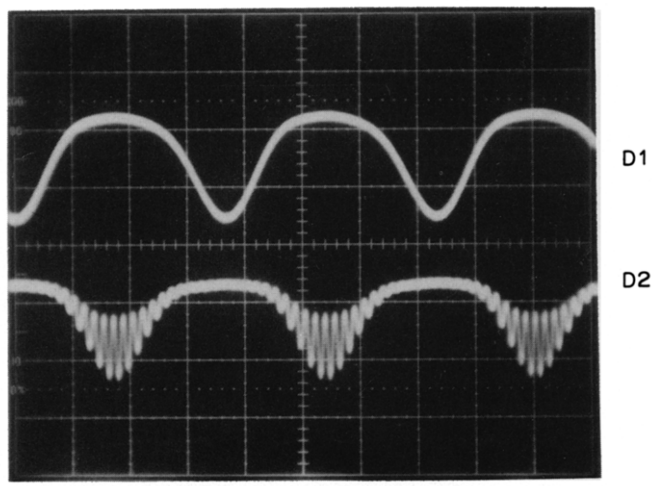

Figure 14. Signals of the photodiodes D1 and D2. The signal of photodiode D1 is used to check the disintegration process. The signal of photodiode D2 represents the Doppler signals of the droplets.

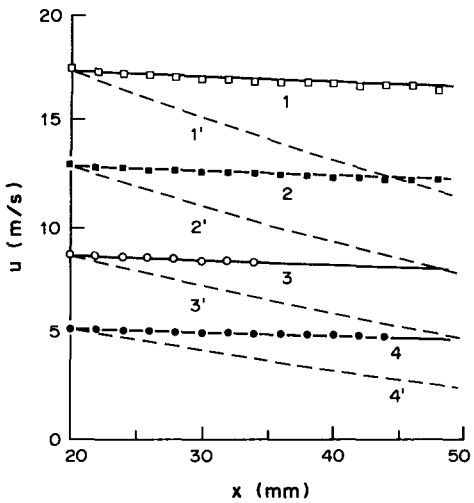

Figure 15. Droplet velocity u as a function of the distance x from the generator exit for different initial velocities. The symbols represent the results of the measurements: ——, numerical calculations for droplets in an infinite chain of droplets; – – –, results for a single droplet with the same initial velocity.

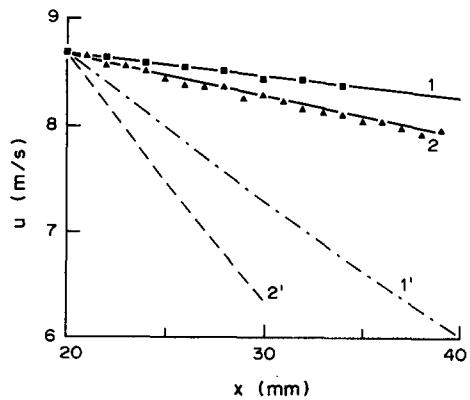

Figure 16. Droplet velocity u as a function of the distance x from the generator exit for two different droplet diameters. The symbols represent the results of the measurements: ——, numerical calculations for droplets in an infinite chain of droplets; – – –, results for a single droplet with the same initial velocity.

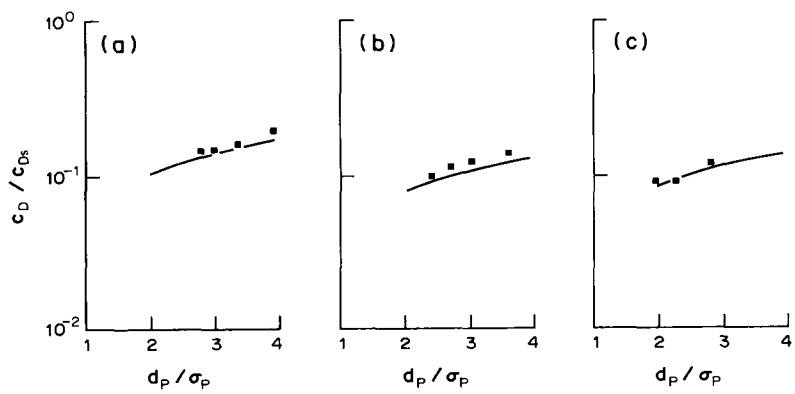

Figure 17. Ratio of the drag coefficient c_D of a droplet in an infinite chain of droplets and the drag coefficient c_{Ds} of a single droplet as a function of the dimensionless droplet spacing d_P/σ_P. The symbols represent the results of the measurements: ——, results of the numerical calculations.

between experiment and theory is observed, which increases with the droplet velocity. This is due to the increasing influence of the pressure gradient within the tube. In the numerical calculations the pressure was assumed to be constant.

The exact alignment of the droplet stream with the axis of the tube is very difficult. It has been observed that misalignment of the droplet streams leads to an increase in the drag. This may be an explanation for the fact that the measured velocities tend to be slightly below the values predicted by the numerical calculations. A comparison of the drag of droplets in an infinite chain of monodisperse droplets with the drag of a single droplet in an unconfined parallel flow shows a drastic decrease in drag for the droplets in the droplet chain. From this point of view a very satisfying prediction of the behavior of the droplets in our experiments has been obtained via the numerical calculations.

In figure 17 the ratio of the drag coefficient c_D of a doplet in an infinite chain of droplets to the drag coefficient c_{Ds} of a single droplet in an unconfined parallel flow is plotted vs the dimensionless droplet spacing d_P/σ_P. One can see that the drag coefficient obtained in the experiments increases with increasing droplet spacing, as predicted by the numerical calculations. Within each set of measurements in figure 17 the orifice diameter d_G and the radius R of the tube was constant. The dimensionless spacing d_P/σ_P was changed by variation of the excitation frequency of the droplet generator. Under these conditions the droplet diameter and droplet spacing change according to [37] and [39].

6. CONCLUSIONS

The purpose of the present investigation was the calculation of drag coefficients and the study of the flow field around an infinite sequence of spheres moving along a straight line. The solution has been obtained by dividing the flow field into two regions: the inner domain, where the flow is influenced strongly by the spheres; and the outer domain, where the flow is essentially parallel to the axis. In the outer domain the velocity distribution is the same as the distribution produced by a rod moving along the axis. The extension of the inner domain had to be determined by numerical calculations. It can be shown that for the range of parameters considered in the present paper, the inner domain is small compared to the tube diameter. Numerical calculations have been used to predict the decrease in droplet velocity in a monodisperse droplet chain obtained by a vibrating orifice droplet generator. It can be shown that the drag coefficient of droplets in an infinite droplet chain is up to an order of magnitude smaller than the drag coefficient of a single droplet in an unconfined parallel flow. The measurements are in good agreement with the numerical results.

REFERENCES

ANDERS, K. & FROHN, A. 1984 Experimental investigation of droplet evaporation in a wide Knudsen number range. In *Proc. 14th Int. Symp. on Rarefied Gas Dynamics* (Edited by OGUCHI, H.), pp. 975–982. Tokyo Univ. Press, Tokyo.

BERGLUND, R. N. & LIU, B. Y. H. 1973 Generation of monodisperse aerosol standards. *Envir. Sci. Technol.* **7**, 147–153.

DEBOOR, C. 1978 *A Practical Guide to Splines*. Springer, New York.

CURRY, H. B. & SCHOENBERG, I. J. 1966 The fundamental spline functions and their limits. *J. Analyse math.* **17**, 71–107.

FENG, K. 1978 *The Methods of Numerical Calculations*. National Defence Printing Office, Beijing.

GOSMAN, A. D., PUN, W. M., PUNCHAL, A. K., SPALDING, D. B. & WOLFSTEIN, M. 1969 *Heat and Mass Transfer in Recirculating Flows*. Academic Press, London.

KÖNIG, G., ANDERS, K. & FROHN, A. 1986 A new light scattering technique to measure the diameter of periodically generated moving droplets. *J. Aerosol Sci.* **17**, 157–167.

LEE, K. C. 1979 Aerodynamic interaction between two spheres at Reynolds numbers around 10^4. *Aeronaut. Q.* **30**, 371–385.

MUNTZ, E. P., QUIAN, S.-S. & DIXON, M. 1984 The injection of liquids into high vacuum for R.G.D. and space applications. In *Proc. 14th Int. Symp. on Rarefied Gas Dynamics* (Edited by OGUCHI, H.), pp. 919–935. Tokyo Univ. Press, Tokyo.

OSEEN, C. W. 1910 Über die Stokes'sche Formel und über eine verwandte Aufgabe in der Hydrodynamik. *Ark. Mat. Astr. Fys.* **6,** No. 29.

PEI, D. C. T. & HAYWARD, G. 1983 Local heat transfer rates from two adjacent spheres in turbulent flow. *Int. J. Heat Mass Transfer* **26,** 1547–1556.

RIMON, Y. & CHENG, S. J. 1969 Numerical solution of a uniform flow over a sphere at intermediate Reynolds numbers. *Phys. Fluids* **12,** 949–959.

ROACHE, P. J. 1976 *Computational Fluid Dynamics.* Hermosa, Albuquerque, N.M.

STOKES, G. G. 1851 On the effect of internal friction of fluids on the motion of pendulums. *Trans. Cambr. phil. Soc.*, **9,** Part II, 8–106.

TSUJI, Y., MORIKAWA, Y. & TERASHIMA, K. 1982 Fluid-dynamic interaction between two spheres. *Int. J. Multiphase Flow* **8,** 71–82.